



SMART-1

AMIE / SIR

Advanced *M*oon micro-*I*mager *E*xperiment
SMART-1 *I*nfrared *S*pectrometer

Document title:	Optimizing the parameters of the AMIE-SIR co-alignment
Document number:	S1-AMIE-RSSD-TN-010
Issue/Revision:	1/-
Date:	2008-Feb-05

	Function	Name
Prepared by	AMIE / SIR Liaison Scientist AMIE Co-I	Björn Grieger Detlef Koschny

Document change record			
Iss./Rev.	Date	Pages affected	Description
D	2007-Jul-31	All	Draft completed
1	2008-Feb-05	19-20	Added description of SPICE kernel update

Contents

1	General items	2
1.1	Scope	2
1.2	Introduction	2
1.3	Brief summary of results	3
1.4	Reference documents	3
1.5	Abbreviations	4
2	Data used	4
2.1	AMIE images	4
2.2	SIR lightcurves	5
3	Estimating the translations imposed by the slews	6
3.1	Maximising the correlation	6
3.2	Slew 1	6
3.3	Slew 2	7
3.4	Slew 3	7
3.5	Slew 4	8
4	Optimising the SIR FOV parameters	11
4.1	The simulation of SIR lightcurves	11
4.2	Slew 1	12
4.3	Slew 2	12
4.4	Slew 3	12
4.5	Slew 4	16
4.6	Finding the optimum parameters	16
5	Update of the SPICE kernel	19

1 General items

1.1 Scope

The SMART-1 spacecraft carried a number of scientific instruments, with some of them being remote sensing instruments. In particular, there are two instruments with relatively small FOVs, where the knowledge of the co-alignment is important:

- The Advanced Moon micro-Imager Experiment (AMIE), a camera with 5.4° field of view and a total of eight fixed filters in front of its CCD detector and
- the SMART-1 Infrared Spectrometer (SIR), an infrared spectrometer with one pixel of 1.11 mrad size.

Initially, it was planned to co-align SIR with the near-IR filter of AMIE. After a detailed study of the image orientation of AMIE it became clear that SIR was co-aligned with the clear filter area of AMIE (called ‘NONE’). In April and May 2004, two dedicated observing campaigns were conducted to study the co-alignment of these two instruments. This was done by scanning the Moon through the assumed field of view of SIR, while taking a few images with AMIE. SIR was acquiring spectra continuously. Comparing the response of SIR versus time with the position and spatial brightness distribution of the Moon in the AMIE images allows the determination of the precise area in the AMIE ‘NONE’ filter to which SIR is responsive.

1.2 Introduction

In this work, we use selected images from the AMIE-SIR co-alignment observation of AMIE and the lightcurves from SIR measurements performed on 04 May 2004 and determine the SIR pointing direction and FOV width within the AMIE frame. The spacecraft was commanded such that the Moon first moves horizontally through the AMIE frame crossing the suspected FOV of SIR and then vertically. For each orientation, one forward and one backward slew was performed, yielding four slews in total. Similarly to the previous analysis [S1-AMIE-RSSD-TN-003], we employ a two step procedure:

1. We estimate the translation imposed by the SC slews from the positions of the Moon in the actually acquired AMIE frames and use this translation to interpolate the theoretical position of the Moon in the AMIE frame over time assuming a constant slew velocity.
2. The parameters of the SIR FOV are adjusted in a way that the expected SIR response caused by the theoretical movement of the Moon through the AMIE frame matches the actually measured SIR lightcurve.

In both steps, we use a more comprehensive approach than the previous analysis. The differences are in detail:

	[S1-AMIE-RSSD-TN-003]	This study
FOV x-position in pixels	95.5	93.2
FOV y-position in pixels	125.5	124.9
FOV diameter in pixels	(12.6)	10.4

Table 1: Comparison of the values found for the SIR FOV parameters by the old analysis [S1-AMIE-RSSD-TN-003] and by this study. The diameter of the SIR FOV was fixed by the former (therefore enclosed in parentheses here), while it was estimated from the data by the latter. The estimated value given is the 2σ diameter of the assumed Gaussian profile, thus it corresponds to $\sigma = 2.6$, cf. Eq. (11).

Ad 1. In the previous analysis, a circle was fitted to the limb of the Moon in order to estimate the position of its centre in the AMIE frame. Herein, we compare the complete spatial brightness pattern of the Moon from two images and search for the optimum translation which maximises the correlation between the two images. This allows us to incorporate an image where the Moon's disk is not completely inside the AMIE frame. This image had to be dismissed previously, as no circle could be fitted to the incomplete limb.

Ad 2. The method used to fit the co-alignment parameters differs in two aspects:

- Previously, only the instant times of ingress and egress of the Moon visible in the SIR lightcurves were used. Herein, we use the continuous brightness variation observed, not only at ingress and egress, but also while the SIR FOV crosses the Moon's disk (as long as the respective AMIE pixels are not saturated).
- Previously, it was assumed that the SIR FOV has a rigid limb with a well defined known width. Herein, we assume that the SIR responsivity has a Gaussian profile with an unknown width. The location *and* width of the SIR FOV within the AMIE frame are estimated from the data.

1.3 Brief summary of results

The values we have found for the parameters of the SIR FOV within the AMIE frame are only slightly different from the results of the previous analysis [S1-AMIE-RSSD-TN-003]; they are compared in Table 1.

1.4 Reference documents

S1-AMIE-RSSD-TN-001 AMIE detector orientation in s/c coordinate system
(Iss./Rev. 1d, 2004-Jan-30)

S1-AMIE-RSSD-TN-002 Selection of images for the AMIE-SIR Co-Alignment
(Iss./Rev. 1-, 2004-Sep-16)

Slew	Images used
1	2, 4
2	6, 7
3	10, 11
4	14, 15

Table 2: Images used herein for the co-alignment analysis, cf. Fig. 1.

S1-AMIE-RSSD-TN-003 AMIE-SIR Co-Alignment analysis (Iss./Rev. 1c, 2004-Oct-24)

1.5 Abbreviations

AMIE	Advanced Moon Imaging Experiment
CCD	Charge Coupled Device
FOV	Field Of View
IR	infrared
SC	Spacecraft
SIR	SMART-1 Infrared Spectrometer

2 Data used

The AMIE-SIR co-alignment observation was originally planned for 2004-Apr-04, but was unsuccessful at that occasion. The observation was successfully repeated on 2004-May-04. Four slews were performed. During each slew, SIR observed for 240 seconds and four images were acquired by AMIE at fixed times relative to the start time of the SIR lightcurves.

2.1 AMIE images

During the AMIE-SIR co-alignment observation, sixteen images in total were acquired. We use the raw images from ‘S1-X-AMIE-2-EDR-RAW-V1.0’. All the images are shown in Fig. 1. Note that the images are displayed in real world orientation, not in CCD coordinates, cf. [S1-AMIE-RSSD-TN-001]. Only a subset of these images was selected for co-alignment analysis. For a discussion of this selection see [S1-AMIE-RSSD-TN-002]. The first image of each slew was dismissed and also image 3 with its obvious deficiency.

For the previous analysis [S1-AMIE-RSSD-TN-003], slew 1 was not used at all, because the algorithm to estimate the position of the centre of the moon did only work for full disk images, and with only one such image for slew 1, the slew parameters could not be constrained.

Herein, we have also used slew 1, as our method to estimate the translation imposed by the slew works also for fractional images. If more than one image was available for a slew, we used the two images which encompass the crossing of the SIR FOV over the Moon’s disk. For a discussion of the slew stability, see [S1-AMIE-RSSD-TN-003]. Table 2 lists the images used.

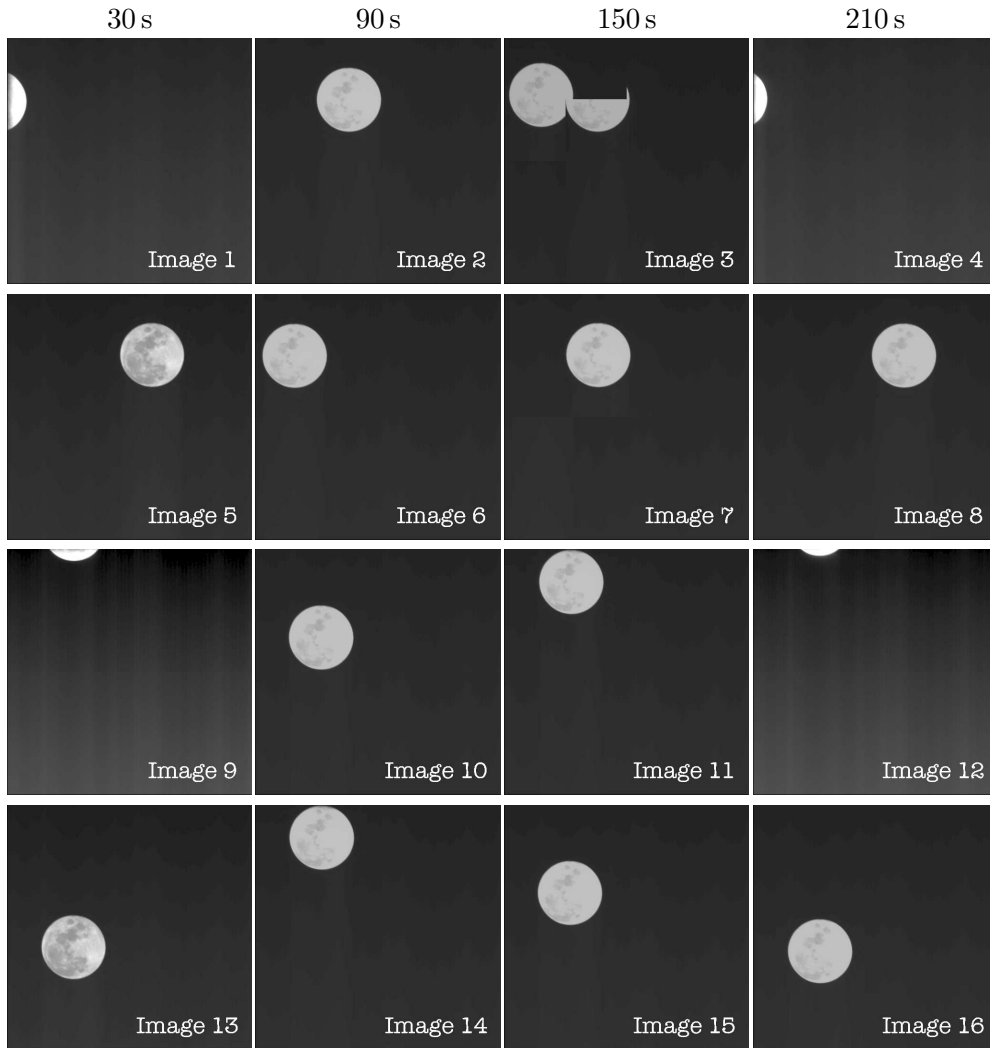


Figure 1: The sixteen images acquired during the AMIE-SIR co-alignment observation. Each slew is represented in one row. At the top the timing of the images with respect to the start of the SIR lightcurve for each slew is given. The first image of each slew had erroneously been overwritten by an image resultant from CCD cleaning prior to image 4, cf. [S1-AMIE-RSSD-TN-002].

2.2 SIR lightcurves

The SIR lightcurves are provided by the SIR team in relative units, scaled to minimum zero and maximum unity. For each slew, the lightcurve covers 240 s with a time resolution of 0.1 s. We refrain from displaying the lightcurves in this section, as they are shown together with simulated lightcurves based on AMIE images in section 4.

3 Estimating the translations imposed by the slews

3.1 Maximising the correlation

To estimate the translation of the Moon's location in the AMIE frame between two images, we perform a brute force search. The translation is described by two parameters, the horizontal offset Δx and the vertical offset Δy . If a certain feature — e. g., the centre of the Moon's disk — is located at (x_1, y_1) in the first image of a slew, it is located at

$$x_2 = x_1 + \Delta x, \quad (1)$$

$$y_2 = y_1 + \Delta y \quad (2)$$

in the second image of the slew. Note that we perform our computations in CCD coordinates, i. e. referring to the images in real world coordinates, cf. Fig. 1, y is increasing from top to bottom.

We systematically scan the two-dimensional parameter space of Δx and Δy and compute the correlation between the two images for each translation. The complete overlapping region of the two images is taken into account. We restrict ourselves to full pixel number shifts for Δx and Δy , thus no interpolation is needed to compute the correlation. Of course the result can not be more accurate than one pixel, but this is a higher accuracy than can be expected for the co-alignment and therefore sufficient.

Knowing the translation $(\Delta x, \Delta y)$ and assuming a constant slew velocity, we can interpolate in time and compute the expected temporal brightness variations at any position (x_0, y_0) of the AMIE CCD. Let t_i be the time at which image i was taken and Δt the time difference between the two images used for the slew, cf. Table 2. At time t during a slew, the position (x_0, y_0) is shifted to the following location in image i :

$$x_i(t) = x_0 - \Delta x \frac{t - t_i}{\Delta t}, \quad (3)$$

$$y_i(t) = y_0 - \Delta y \frac{t - t_i}{\Delta t}. \quad (4)$$

Note that this equation holds for both images of the slew, i. e., also for $t < t_i$. The brightness expected for the position (x_0, y_0) at time t is just the brightness of image i at $(x_i(t), y_i(t))$, that is, $B_i(x_i(t), y_i(t))$. We can simulate two lightcurves for each slew because we can use either of the two images. The two lightcurves should be identical for a perfect correlation. Just as example, we show below simulated lightcurves for the point $(x_0 = 95.5, y_0 = 124.5)$, the centre of the SIR FOV as estimated by [S1-AMIE-RSSD-TN-003]. The value for B_i is not interpolated between pixels; we just take the nearest pixel.

3.2 Slew 1

We consider images 2 and 4, cf. Fig. 1. They were taken at 90 s and 210 s with respect to the start time of the SIR lightcurve. The maximum correlation is found for the translation

$$\begin{aligned} \Delta x &= -233, \\ \Delta y &= -2. \end{aligned} \quad (5)$$

0.849798 0.876752 0.898044 0.909572 0.910077 0.901327 0.887663
0.851786 0.880850 0.905164 0.918917 0.917743 0.905957 0.889992
0.852360 0.882842 0.909609 0.926119 0.923349 0.908780 0.891184
0.851766 0.882690 0.910556 0.929201 0.926192 0.910009 0.891609
0.850313 0.880780 0.908100 0.926806 0.925709 0.910004 0.891575
0.848036 0.877286 0.902772 0.919692 0.921070 0.908452 0.891038
0.844772 0.872188 0.895148 0.909699 0.912595 0.904242 0.889401

Table 3: Slew 1, correlation values for translations close to the optimum. The optimum translation of $(-233, -2)$ is represented by the centre of the 9×9 matrix, thus the region $\Delta x = [-237 \dots -229]$ and $\Delta y = [-6 \dots 2]$ is shown.

0.972724 0.979095 0.982843 0.982753 0.978889 0.972478 0.964536
0.978682 0.986519 0.991654 0.991647 0.986628 0.978907 0.969856
0.981978 0.991035 0.997630 0.997911 0.991723 0.982841 0.972979
0.981734 0.990844 0.997592 0.998276 0.992190 0.983269 0.973404
0.978133 0.986178 0.991737 0.992436 0.987770 0.980088 0.971062
0.971968 0.978715 0.983032 0.983593 0.980252 0.974085 0.966280
0.964150 0.969806 0.973228 0.973706 0.971259 0.966343 0.959716

Table 4: Slew 2, correlation values for translations close to the optimum. The optimum translation of $(115, -2)$ is represented by the centre of the 9×9 matrix, thus the region $\Delta x = [111 \dots 119]$ and $\Delta y = [-6 \dots 2]$ is shown.

Table 3 shows the correlation values in the neighbourhood of the optimum translation. Simulated lightcurves are shown in Fig. 2. The lightcurve simulated from image 4 drops down below 165 s because the Moon's disk is cut off by the edge of the AMIE 'NONE' filter FOV. The excellent agreement of the two lightcurves above 165 s reflects the high correlation between the two images achieved with the optimum translation.

3.3 Slew 2

We consider images 6 and 7, cf. Fig. 1. They were taken at 90 s and 150 s with respect to the start time of the SIR lightcurve. The maximum correlation is found for the translation

$$\begin{aligned}\Delta x &= 115, \\ \Delta y &= -2.\end{aligned}\tag{6}$$

Table 4 shows the correlation values in the neighbourhood of the optimum translation. Simulated lightcurves are shown in Fig. 3. Again we note an excellent agreement between the two images with the optimum translation.

3.4 Slew 3

We consider images 10 and 11, cf. Fig. 1. They were taken at 90 s and 150 s with respect to the start time of the SIR lightcurve. The maximum correlation

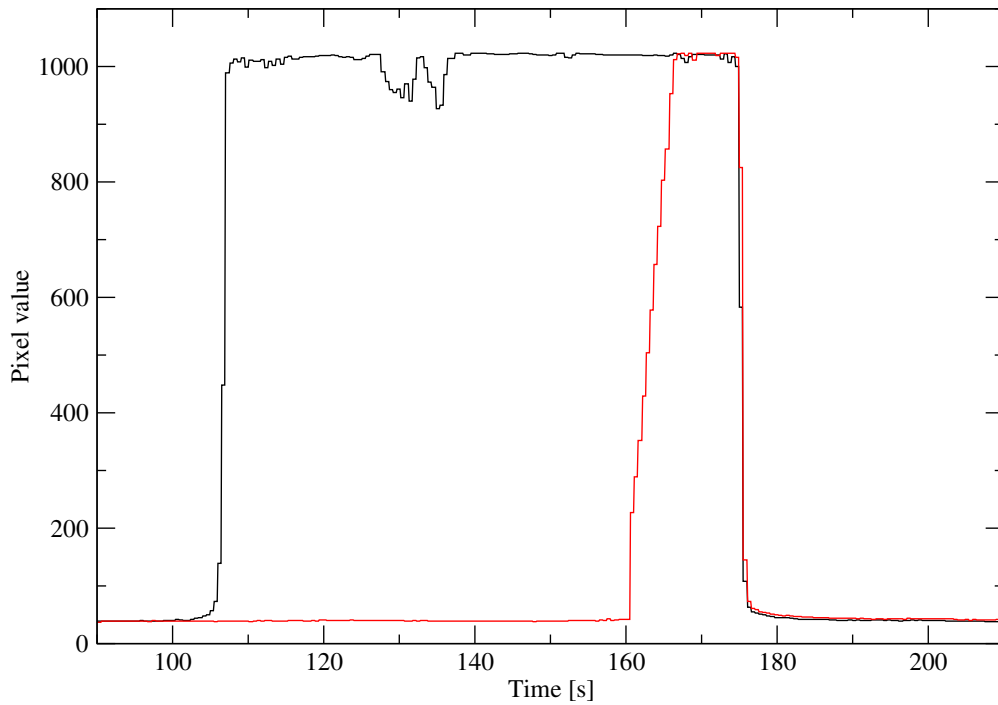


Figure 2: Simulated lightcurves for AMIE pixel position (95.5, 124.5) during slew 1. The black line is based on image 2, the red line is based on image 4, cf. Fig. 1.

is found for the translation

$$\begin{aligned}\Delta x &= 3, \\ \Delta y &= -115.\end{aligned}\tag{7}$$

Table 5 shows the correlation values in the neighbourhood of the optimum translation. Simulated lightcurves are shown in Fig. 4. Like before we note an excellent agreement between the two images with the optimum translation.

3.5 Slew 4

We consider images 14 and 15, cf. Fig. 1. They were taken at 90s and 150s with respect to the start time of the SIR lightcurve. The maximum correlation is found for the translation

$$\begin{aligned}\Delta x &= -1, \\ \Delta y &= 115.\end{aligned}\tag{8}$$

Table 6 shows the correlation values in the neighbourhood of the optimum translation. Simulated lightcurves are shown in Fig. 5. Like before we note an excellent agreement between the two images with the optimum translation.

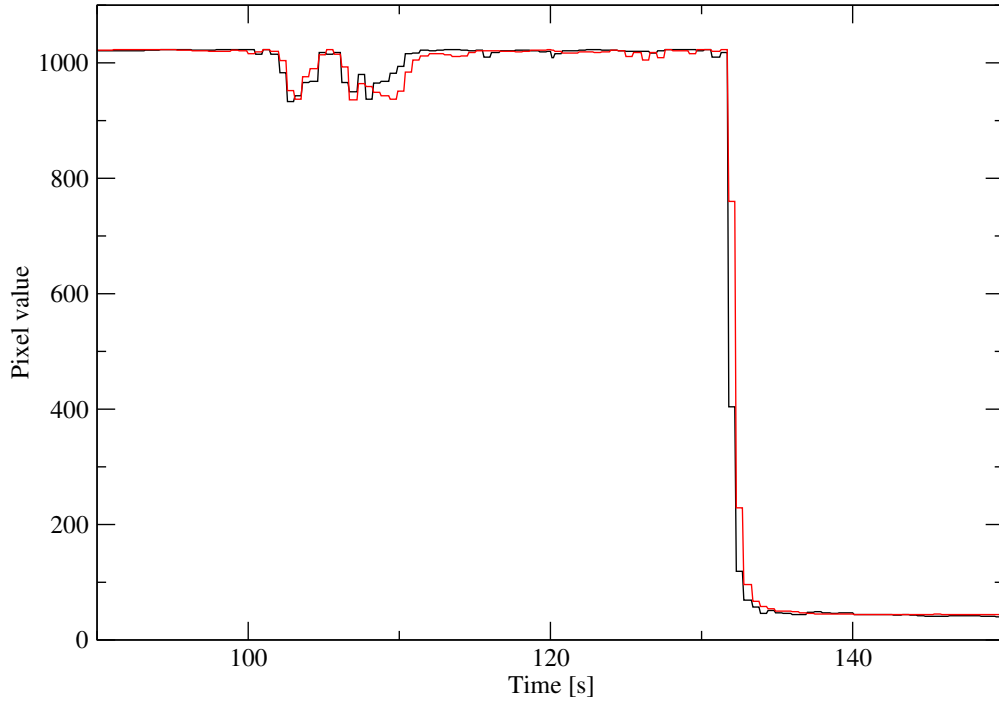


Figure 3: Simulated lightcurves for AMIE pixel position (95.5, 124.5) during slew 2. The black line is based on image 6, the red line is based on image 7, cf. Fig. 1.

```

0.964140 0.970169 0.974176 0.975527 0.973853 0.969539 0.963303
0.970533 0.977787 0.982977 0.984896 0.982764 0.977446 0.970120
0.974990 0.983578 0.990318 0.993135 0.990320 0.983690 0.975130
0.976921 0.986504 0.994648 0.998631 0.995152 0.987269 0.977748
0.976038 0.985702 0.993965 0.998303 0.995085 0.987118 0.977550
0.972435 0.981253 0.988352 0.991897 0.989652 0.983052 0.974447
0.966632 0.974276 0.980032 0.982704 0.981192 0.976153 0.968912

```

Table 5: Slew 3, correlation values for translations close to the optimum. The optimum translation of (3, -115) is represented by the centre of the 9×9 matrix, thus the region $\Delta x = [-1 \dots 7]$ and $\Delta y = [-119 \dots -111]$ is shown.

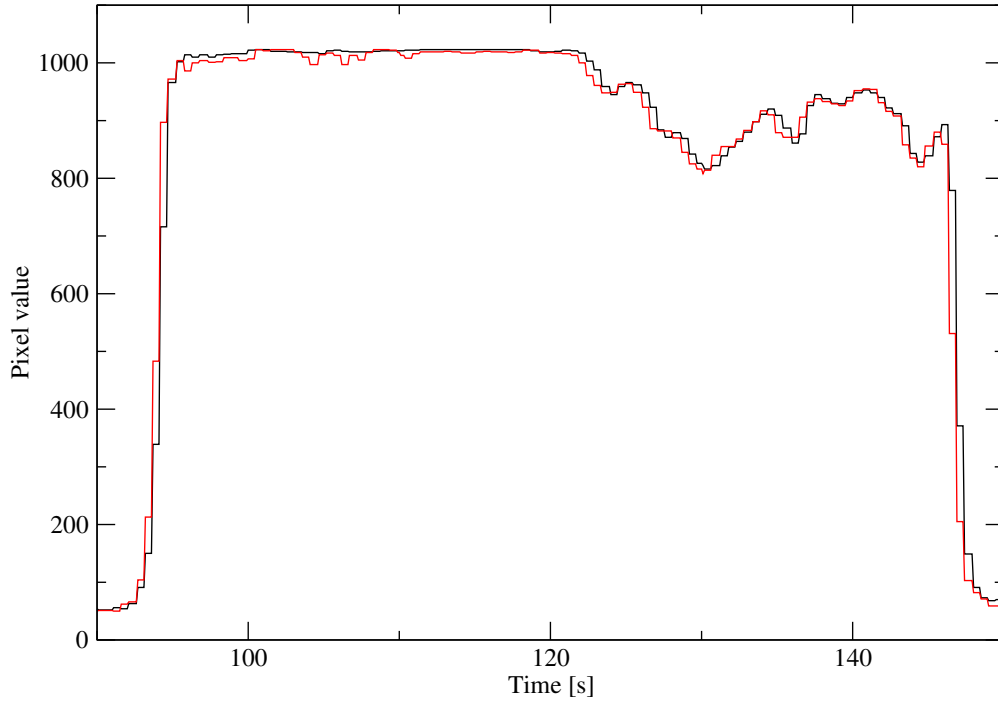


Figure 4: Simulated lightcurves for AMIE pixel position (95.5, 124.5) during slew 3. The black line is based on image 10, the red line is based on image 11, cf. Fig. 1.

```

0.969148 0.976315 0.981214 0.982519 0.979581 0.973693 0.965991
0.974753 0.983299 0.989759 0.991703 0.987827 0.980600 0.971727
0.977922 0.987451 0.995278 0.998098 0.993363 0.984975 0.975288
0.978197 0.987662 0.995394 0.998481 0.994083 0.985809 0.976209
0.975604 0.984085 0.990564 0.993084 0.989898 0.983001 0.974357
0.970606 0.977845 0.983023 0.984953 0.982731 0.977368 0.970033
0.963807 0.969940 0.974127 0.975663 0.974071 0.969897 0.963777

```

Table 6: Slew 4, correlation values for translations close to the optimum. The optimum translation of $(-1, 115)$ is represented by the centre of the 9×9 matrix, thus the region $\Delta x = [-5 \dots 3]$ and $\Delta y = [111 \dots 119]$ is shown.

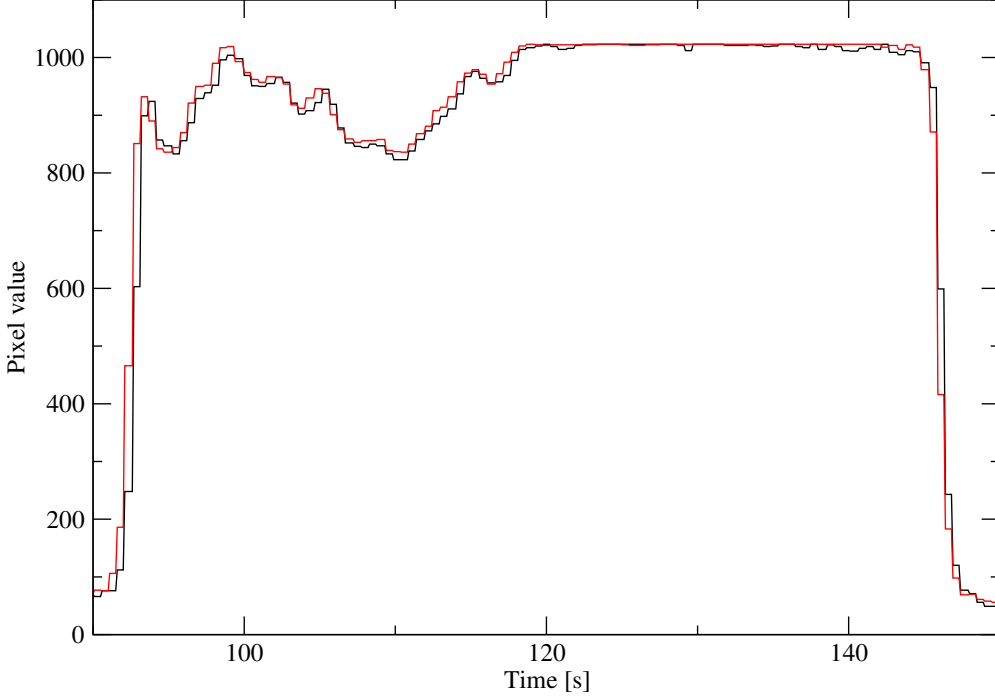


Figure 5: Simulated lightcurves for AMIE pixel position (95.5, 124.5) during slew 4. The black line is based on image 14, the red line is based on image 15, cf. Fig. 1.

4 Optimising the SIR FOV parameters

4.1 The simulation of SIR lightcurves

Given the parameters of each slew, we can simulate lightcurves of expected brightness variations for each point on the AMIE CCD, as has been demonstrated in section 3. We now extend this simulation procedure and consider not just a single point, but a weighted sum of pixels representing the SIR FOV.

Let — like in section 3.1 — t_i be the time at which image i was taken and Δt the time difference between the two images used for the slew, cf. Table 2. If the centre of the SIR FOV on the AMIE CCD is located at $(x_{\text{SIR}}, y_{\text{SIR}})$, then at time t during a slew, this centre is shifted to

$$x_i(t) = x_{\text{SIR}} - \Delta x \frac{t - t_i}{\Delta t}, \quad (9)$$

$$y_i(t) = y_{\text{SIR}} - \Delta y \frac{t - t_i}{\Delta t}. \quad (10)$$

We assume that the SIR FOV can be represented by a radially symmetric Gaussian profile with its width described by σ_{SIR} . If $B_i(x, y)$ is the brightness

	Set 1	Set 2
x_{SIR}	95.5	93.2
y_{SIR}	125.5	124.9
σ_{SIR}	2.7	2.6

Table 7: The two sets of SIR FOV parameters which have been used to simulate the lightcurves shown herein. Set 1 represents the findings of the previous analysis [S1-AMIE-RSSD-TN-003], however, we did not employ the fixed FOV width used therein but an optimised σ_{SIR} to enable a fair comparison with set 2, which represents the optimum results found by the present study.

of image i at pixel (x, y) , the simulated SIR brightness at time t is

$$B_i(t) = \sum_{\text{Pixel}(x,y)} B_i(x, y) e^{-\frac{(x-x_i(t))^2+(y-y_i(t))^2}{\sigma_{\text{SIR}}^2}}. \quad (11)$$

We use only pixels which are not saturated, i. e., which have a data number lower than 1000. The simulated brightness $B_i(t)$ becomes insignificant if it is based on only a small number of valid pixel. We discard a time point $B_i(t)$ if the sum taken over all valid pixels is

$$\sum_{\text{Pixel}(x,y)} e^{-\frac{(x-x_i(t))^2+(y-y_i(t))^2}{\sigma_{\text{SIR}}^2}} < \frac{\pi \sigma_{\text{SIR}}^2}{e}. \quad (12)$$

The resultant lightcurves are scaled to the same mean and variance as the observed lightcurve (considering only valid time points). Below, we simulate lightcurves for two sets of SIR FOV parameters, which are listed in Table 7. The method to find the optimum set of parameters, set 2, is described in section 4.6.

4.2 Slew 1

The simulated lightcurves for slew 1 are shown in Fig. 6. Slew 1 is towards positive x -direction, thus moving the centre of the SIR FOV from $x = 95.5$ to $x = 93.2$ shifts the simulated lightcurves to later times, yielding a better correlation with the observed light curve, particularly at egress.

4.3 Slew 2

The simulated lightcurves for slew 2 are shown in Fig. 7. Slew 1 is towards negative x -direction, thus moving the centre of the SIR FOV from $x = 95.5$ to $x = 93.2$ shifts the simulated lightcurves to earlier times. In the case of slew two, this slightly worsens the correlation with the observed light curve.

4.4 Slew 3

The simulated lightcurves for slew 3 are shown in Fig. 8. Slew 3 is towards positive y -direction (downward in real world orientation). The SIR FOV crosses the Moon left of its centre, thus moving the centre of the SIR FOV from $x = 95.5$

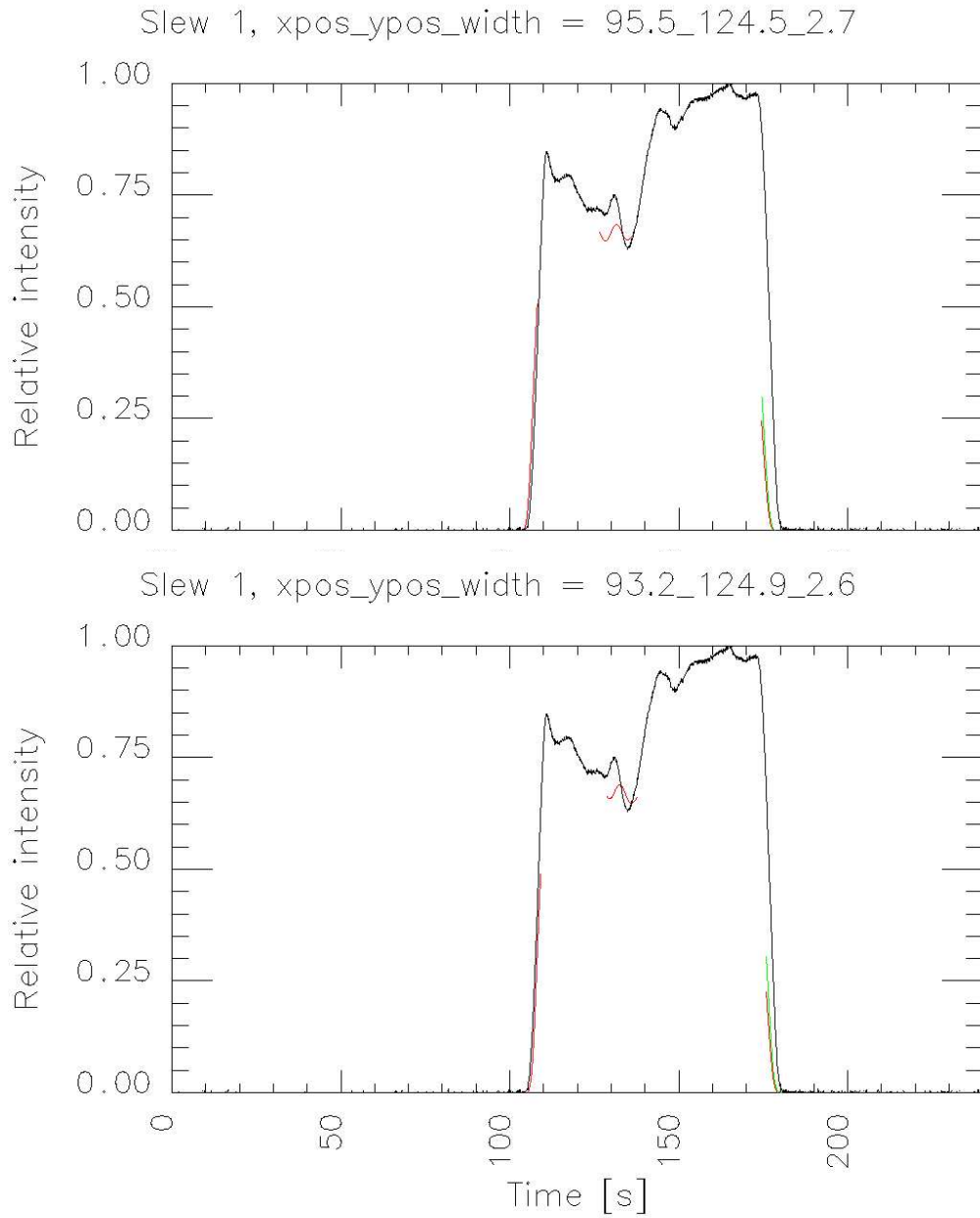


Figure 6: Observed (black) and simulated (red from image 2 and green from image 4, cf. Table 2) SIR lightcurves for slew 1. *Top*: parameter set 1; *Bottom*: parameter set 2; cf. Table 7. Simulated lightcurves are only plotted where enough non-saturated AMIE pixels are available.

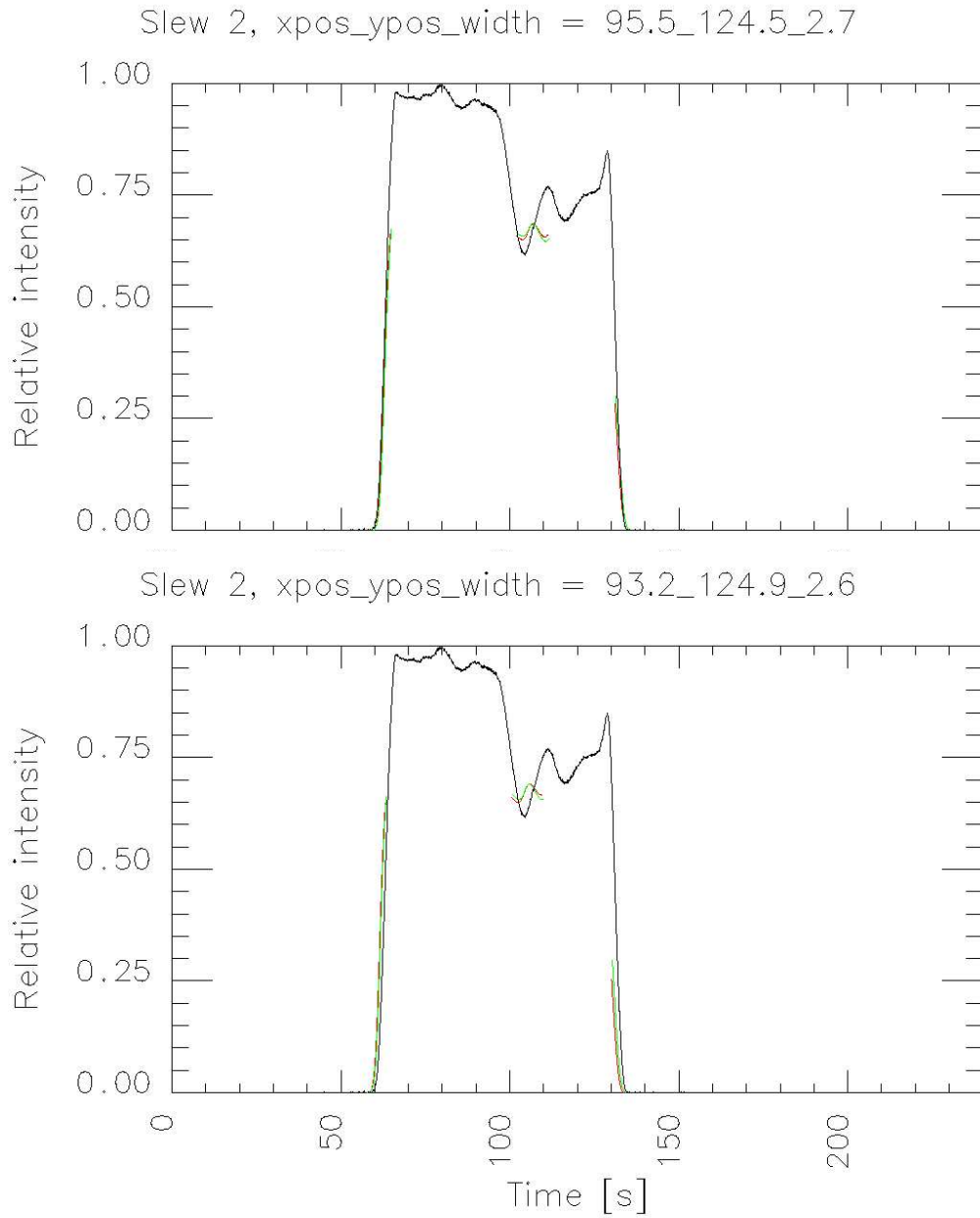


Figure 7: Observed (black) and simulated (red from image 6 and green from image 7, cf. Table 2) SIR lightcurves for slew 2. *Top*: parameter set 1; *Bottom*: parameter set 2; cf. Table 7. Simulated lightcurves are only plotted where enough non-saturated AMIE pixels are available.

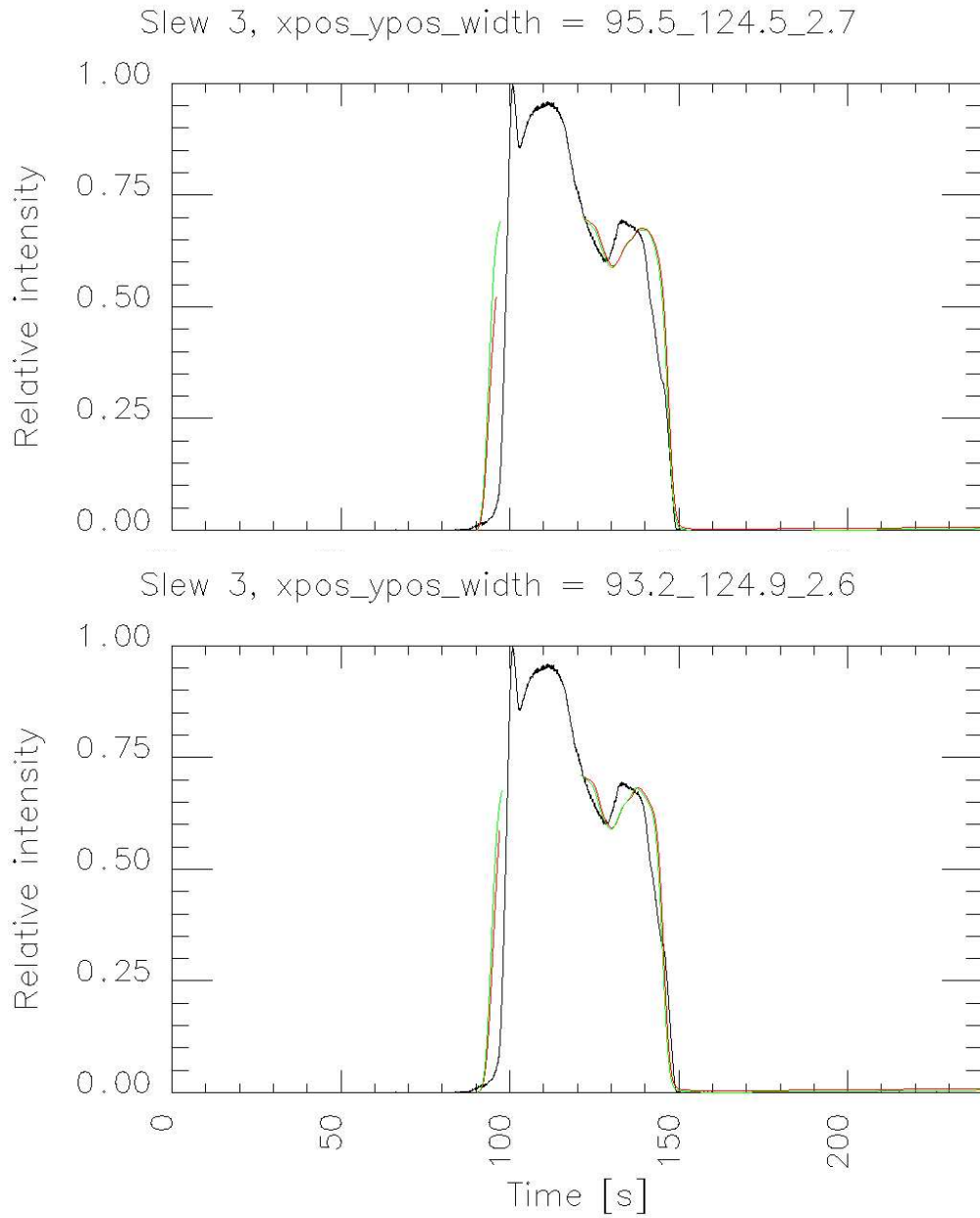


Figure 8: Observed (black) and simulated (red from image 10 and green from image 11, cf. Table 2) SIR lightcurves for slew 3. *Top*: parameter set 1; *Bottom*: parameter set 2; cf. Table 7. Simulated lightcurves are only plotted where enough non-saturated AMIE pixels are available.

to $x = 93.2$ shifts the transect even further away from the Moon's centre and narrows the lightcurve in time. This clearly increases the correlation with the observed light curve.

4.5 Slew 4

The simulated lightcurves for slew 4 are shown in Fig. 9. Slew 4 is towards negative y -direction (upward in real world orientation). Similarly to slew 3, the SIR FOV crosses the Moon left of its centre, thus moving the centre of the SIR FOV from $x = 95.5$ to $x = 93.2$ shifts the transect even further away from the Moon's centre and narrows the lightcurve in time, by this increasing the correlation with the observed light curve.

4.6 Finding the optimum parameters

The optimum parameter values of set 2 and the optimum σ value of set 1, cf. Table 7, have been found by brute force searches. We have scanned the parameter space with a resolution of 0.1 pixels, thus this is the theoretical maximum accuracy of the results. The real accuracy to which the results are constrained by the available data is of course much lower, as discussed below.

For each point of the parameter space, we simulate two lightcurves (for the two AMIE images used) per slew, thus eight lightcurves in total. Then we compute the total correlation between observed and simulated lightcurves, considering only valid simulated time points, cf. section 4.1. The correlation achieved with parameter set 1 is 0.955.

In Fig. 10 we show the correlation in dependence on the SIR FOV centre position for a fixed FOV width corresponding to $\sigma = 2.6$, cf. Eq.(11). The maximum correlation of 0.970 is achieved with parameter set 2 as given in Table 7.

The width of the correlation maximum as shown in Fig. 10 gives an idea of the accuracy of the retrieved location of the SIR FOV. The position seems to be more constrained in x -direction — within a few pixels —, while the correlation is less peaked in y -direction, constraining the location in this direction within 5 to 10 pixels. In this respect, the result of the previous analysis [S1-AMIE-RSSD-TN-003], cf. Table 1, is within the range of uncertainty.

When comparing lightcurves simulated based on the optimised SIR FOV parameters — set 2 — with the observed ones, we still note some deviations. For slew 1 and 2 (Figs. 6, 7), the small sections of the simulated lightcurves within the Moon's disk are too dark. This could be due to included bright pixels which are already close to saturation and not behaving linearly or to the exclusion of saturated pixel which introduces a bias towards darker values.

The timing of ingress and egress and also of small variations inside the Moon's disk does not match perfectly. This can only partly be attributed to geometric distortions of the camera, which have not yet been taken into account. The fact that the match between the two lightcurves simulated from different images is in general better than the match between simulated and observed lightcurves indicates that there must be another cause for the remaining incon-

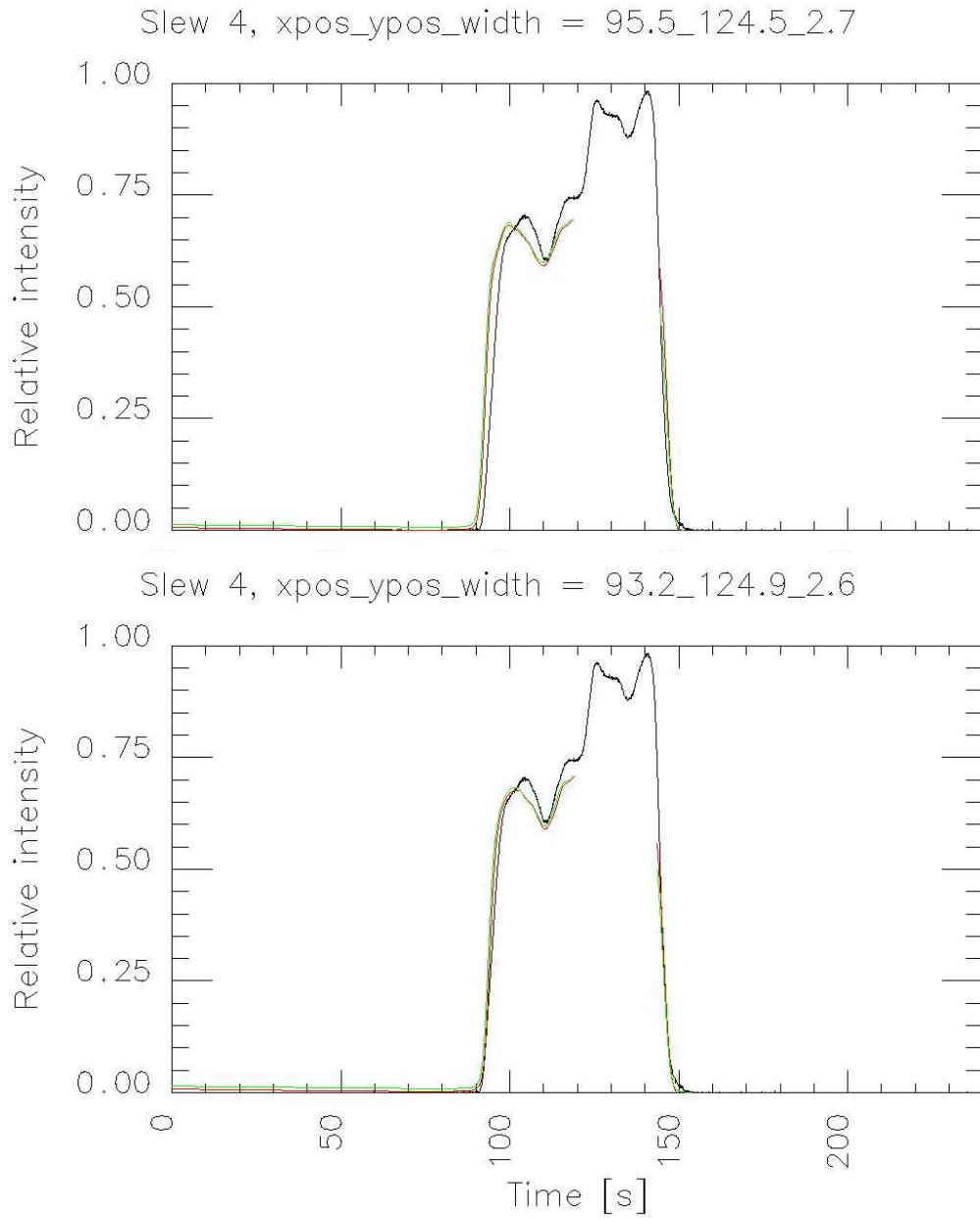


Figure 9: Observed (black) and simulated (red from image 14 and green from image 15, cf. Table 2) SIR lightcurves for slew 4. *Top*: parameter set 1; *Bottom*: parameter set 2; cf. Table 7. Simulated lightcurves are only plotted where enough non-saturated AMIE pixels are available.

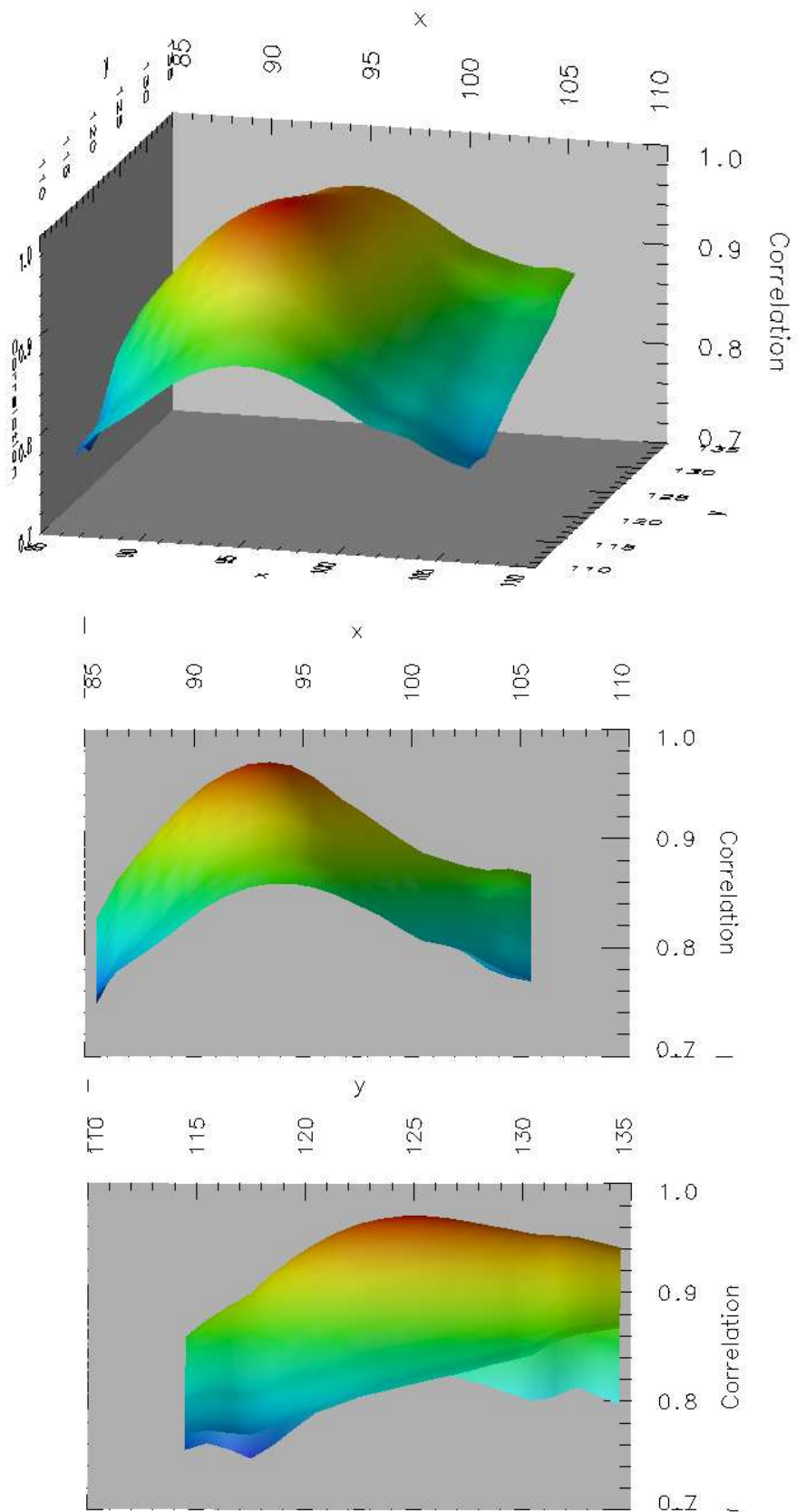


Figure 10: Correlation between lightcurves observed by SIR and simulated from AMIE images in dependence on the assumed position of the SIR FOV centre on the AMIE CCD.

sistencies. Possibly they are due to the different spectral response of SIR and the AMIE 'NONE' filter.

5 Update of the SPICE kernel

The SIR boresight with respect to the SC frame has previously been determined in the SPICE kernel

```
SMART1_V1.TF
```

To take into account the optimized parameters of the AMIE-SIR co-alignment, we use SPICE to compute the new SIR boresight vector in the SC frame. Below is a log of this computation:

```
Old SIR boresight in SMART1-SIR frame
```

```
-----  
0.  0. 180.
```

```
Old SIR boresight in SC frame (normalized to z=1)
```

```
-----  
-0.000610865314  0.000436332341  1.
```

```
AMIE NONE filter boresight in SMART1_AMIE_NONE frame
```

```
-----  
0.  0.  1.
```

```
AMIE NONE filter FOV corners in SMART1_AMIE_NONE frame
```

```
-----  
0.0231173718  0.0231173718  0.999465444  
-0.0231173718  0.0231173718  0.999465444  
-0.0231173718 -0.0231173718  0.999465444  
0.0231173718 -0.0231173718  0.999465444
```

```
New SIR boresight in NONE filter pixel co-ordinates
```

```
-----  
93.2 124.9
```

```
New SIR boresight in SMART1_AMIE_NONE frame
```

```
-----  
-0.0146847339 -0.0118165508  0.999465444
```

```
AMIE NONE filter corners in SC frame (normalized to z=1)
```

```
-----  
0.0346637165 -0.0369109404  1.  
0.0346539866  0.00937269252  1.  
-0.0116012882  0.00937269252  1.  
-0.0116209938 -0.0368862736  1.
```

New SIR boresight in SC frame (normalized to z=1)

-0.000302280951 0.000938925493 1.

Old and new SIR boresight in SC frame (unit vectors)

-0.000610865142 0.000436332218 0.999999718
-0.000302280804 0.000938925036 0.999999514

Therefore, the SPICE kernel has to be modified to yield the SIR boresight vector in the SC frame as

(-0.000302280804, 0.000938925036, 0.999999514).